ORIGINAL PAPER

Nonlinear Dynamic Behavior of Longitudinal-Torsional-Lateral Round Balance Rope Combined With Hoisting Rope in Friction Hoisting System

Ning Zhang[1,2] · Guohua Cao[1,2] · Zhencai Zhu[1,2] · Weihong Peng[3]

Abstract

Purpose Mine friction hoisting system mainly consists of rigid body, flexible tensioned hoisting ropes and flexible low-tension balance rope. This study is carried out to reveal the complex coupling dynamic characteristics of hoisting rope with heavy load as well as round balance rope with time-varying bending and torsional curvature in ultra-kilometer deep friction hoisting system.
Methods Coupling relationships among rigid body, hoisting ropes and round balance rope are established through boundary constraint equation. Hoisting ropes on both sides of traction sheave are modeled based on variable-length finite element method. Dynamic model with friction constraint of round balance rope is established through absolute nodal coordinate formulation, the directional cosine matrix, Costello theory along with Coulomb's friction law. Time-varying multi-segments non-equal-length element is used so as to reduce the element number of round balance rope. Then, the extended KDP generalized-α method is used to iteratively solve the nonlinear differential algebraic equations.
Results Non-stationary responses of round balance rope combined with hoisting ropes are investigated when transient resonance occurs in hoisting ropes. The results display that the round balance rope with friction constraint boundary has undergone severe in-plane and out-of-plane large displacement and deformation under the given conditions in this paper.
Conclusion The main reasons that cause large displacement vibration of round balance rope in-plane and out-of-plane directions are long lasting time transient longitudinal resonance of hoisting ropes, high coupling of axial strain with bending and torsional curvature in flexible low-tension round balance rope, intersection between the doubling excitation frequency and longitudinal natural frequency of round balance rope, and twisting force inside round balance rope.

Keywords Round balance rope · Dynamic model · large deformation · Nonlinear dynamics · Friction hoisting system

Notation

$\mathbf{B}^B, \mathbf{B}^H, \mathbf{B}$	Boolean mapping matrix
$\mathbf{C}_{vL}, \mathbf{C}_B(\mathbf{q}_B), \mathbf{C}_{vR}, \mathbf{C}_{eB},$ $\mathbf{C}_{ass}(\mathbf{q}_{ass}), \mathbf{C}_{evL}, \mathbf{C}_{evR}$	Damping matrices
dof1, dof2, dof3	Degrees of freedom
EI	Bending stiffness coefficient
$e^s(t)$	Longitudinal excitation
f_{kg}	Gravity
$\mathbf{F}_{vL}^{ex}, \mathbf{F}_{vR}^{ex}, \mathbf{F}_B^{ex}, \mathbf{F}_{ass}^{ex}$	Generalized external force vectors
$g_1, \ldots\ldots g_{10}$	Bilateral constraint equations
g_1', g_2'	Uilateral constraint equations
H	Height between two conveyances
$\mathbf{I}_4$	Four-order identity matrix
$\mathbf{K}_{vL}, \mathbf{K}_{vR}, \mathbf{K}_{evL}, \mathbf{K}_{evR}$	Stiffness matrix of hoisting rope
l_B, l_2, l_3	Length of rope

✉ Guohua Cao
caoguohua@cumt.edu.cn

1 Jiangsu Province and Education Ministry Co-Sponsored Collaborative Innovation Center of Intelligent Mining Equipment, CUMT, China University of Mining and Technology, Xuzhou 221116, Jiangsu, China

2 School of Mechanical and Electrical Engineering, China University of Mining and Technology, Xuzhou 221116, China

3 School of Mechanics and Civil Engineering, China University of Mining and Technology, Xuzhou 221116, China

l_{eB}, l_{evL}, l_{evR}	Element length
M_{CR}, M_{CL}	Mass of conveyance
$\mathbf{M}_{ass}, \mathbf{M}_{vR}, \mathbf{M}_{vL}, \mathbf{M}_B, \mathbf{M}_{eB}, \mathbf{M}_{evL}, \mathbf{M}_{evR}$	Mass matrices
n_{vR}, n_{vL}, n_B	Number of element
$\mathbf{N}_{vL}, \mathbf{N}_{vR}, \mathbf{N}_B$	Element shape function matrix
$\mathbf{N}'_{vL}, \mathbf{N}'_{vR}, \mathbf{N}'_B, \mathbf{N}''_{vL}, \mathbf{N}''_{vR}, \mathbf{N}''_B$	first, second-order spatial slope of element shape function matrix
$\dot{\mathbf{N}}_{vL}, \dot{\mathbf{N}}_{vR}, \ddot{\mathbf{N}}_{vL}, \ddot{\mathbf{N}}_{vR}$	First, second-order time differentials of element shape function matrix
q_{CR}, q_{CL}	Position coordinate of conveyance
$\mathbf{q}_{vL}, \mathbf{q}_{vR}, \mathbf{q}_B, \mathbf{q}_{ass}, \mathbf{q}_{B,k}, \mathbf{q}_{vL,i}, \mathbf{q}_{vR,i}$	Coordinate vector
$\dot{\mathbf{q}}_{ass}$	Velocity vector
$\ddot{\mathbf{q}}_{ass}$	Acceleration vector
Q_{a1}, Q_{a2}, Q_{a3}	Longitudinal stiffness coefficients
Q_{b1}, Q_{c1}	Longitudinal-torsional coupling stiffness coefficients
Q_{d1}	Torsional stiffness coefficient
$\mathbf{Q}_B(\mathbf{q}_B), \mathbf{Q}_{eB}, \mathbf{Q}_{ass}(\mathbf{q}_{ass})$	Elastic force vectors
R	Radius of traction sheave
S_c	Horizontal distance
$\mathbf{W}_N$	First-order partial derivative of the coordinate of bilateral constraints
$\mathbf{W}_T$	Vector of tangential force direction
μ	Friction coefficient
$\varepsilon_{vL}, \varepsilon_{vR}, \varepsilon$	Axial strain
κ	Bending curvature
τ	Torsional curvature
$\zeta_v; \zeta_B$	Damping coefficient of rope
ρ_1, ρ_2, ρ_3	Linear density of rope
$\mathbf{\Phi}_N, \mathbf{\Phi}_{H,N}, \mathbf{\Phi}_{B,N}$	Bilateral constraint equations
$\mathbf{\Phi}_T$	Uilateral constraint equations
ANCF16LC	Longitudinal-torsional-lateral coupling spatial rope element with 16 degrees of freedom based on absolute nodal coordinate formulation, the directional cosine matrix, and Costello theory
FEMLC	Longitudinal-torsional coupling based on finite element method
RBRSD	Round balance rope suspension device

Introduction

As a throat connecting the underground mine and the ground, the mine hoisting system has extremely high safety requirements and has become a research hotspot for safe operation [1]. Many scholars have studied the mine hoisting system. According to the rope tension, the wire rope in mine hoisting system can be divided into tensioned rope and low-tension rope. The tensioned rope includes hoisting rope in winding hoisting system [2–4] and in friction hoisting system [5], as well as the guide ropes [6, 7]. Low-tension ropes are mainly used as balance ropes [8], travelling cables [9]. According to the cross-section shape of wire rope, the balance rope can be divided into round balance rope and flat balance rope. The flat balance rope is alternately woven together by a plurality of left and right cross-twisted sub-ropes, and has the best non-rotation performance. The round balance rope is made of multiple steel wires and strands. The spiral shape of the internal steel wire will produce torque under the action of axial tension [10]. Round balance rope is often used in metal mine friction hoisting system, and flat balance rope is often used in coal mine friction hoisting system.

Mine hoist is a complex coupling system [11], which includes hoisting rope with time-varying length and balance rope with time-varying curvature, thus its dynamic characteristics are extremely complex. At present, most studies focus on tensioned rope dynamics. These studies are subject to the gravity and external axial load of the tensioned rope, and the deformation is small. The small deformation theory can be used for tensioned rope dynamic modeling. Therefore, based on the small deformation theory, the dynamic model of tensioned rope can be established by the assumed mode method, the natural mode shape method and the finite element method. Cao et al. [12] established the dynamic equation of rope-guided hoisting system according to the Hamilton's principle, the natural mode shape method, as well as Galerkin's method. Wang et al. [13], based on the assumed mode method and Lagrange equation, studied the dynamic response of the multi-cable-driven parallel suspension platform system. Cao et al. [14] studied the dynamic response of rigid guidance hoisting system with time-varying length based on finite element method.

Studies about the low-tension rope is not subjected to external axial loads except its gravity, hence the low-tension rope is slack, which may cause large deformation under the action of small external force. As a result, the

above mentioned small deformation modeling theories will not be able to meet the needs of establishing low-tension rope dynamic model. Shabana et al. [15] proposed the theory of two-dimensional absolute nodal coordinate formulation(ANCF), which can concisely and effectively establish the dynamic model of large deformation motion, and successfully applied it to in-plane dynamic analysis of cantilever beam. Then, three-dimensional absolute nodal coordinate formulation with slope continuity at nodes is proposed for large rotation, torsion and shear deformation analysis of three-dimensional beam [16, 17]. Zhang et al. [18] derived the decoupled strain ANCF cable element. Compared with the traditional model, the decoupled model eliminates the strain coupling effect. Zhang et al. [19] established dynamic model of flat balance rope based on ANCF, and analyzed the dynamic characteristics of the flat balance rope under multiple constraints. Fan et al. [20] proposed a non-singular modeling theory based on quaternion for three-dimensional Euler–Bernoulli beams with large deformation and rotation. Then, the non-singular beam formulation is used to model the travelling cable [21], and the influence of the travelling cable response was studied when excitation was acted on the cable. These scholars only considered the in-plane motion of low-tension rope, and ignored the spatial torsion characteristics of slender beam.

In kilometer-deep well, the weight of single round balance rope will reach several tons or even tens of tons, and the axial deformation is large. At this time, the torsion caused by axial deformation cannot be ignored. Xia et al. [22] gave the relationship of axial force and torsion moment of wire rope with axial strain and torsion strain based on linear stiffness coefficient. However, the scholar only studied the relationship between tension and torsion of wire rope in statics, and did not study the longitudinal-torsional coupling dynamic behavior of wire rope in depth. Based on the absolute coordinate and the directional cosine matrix, Dombrowski [23] developed a three-dimensional large deformation Rayleigh beam element to describe the spatial slender beam with non-negligible torsion effect. Yang et al. [24] proposed a time-varying Rayleigh beam axial element model, and carried out dynamic analysis on the axially moving and rotating cantilever Rayleigh beam. This model can effectively solve the dynamic problems of axially moving and rotating beams. However, the dynamic model of the above scholars did not consider the internal coupling relationship between longitudinal stiffness and torsional stiffness of flexible body.

Round balance rope is connected with conveyance through round balance rope suspension device (RBRSD) in the friction hoisting system. The RBRSD can unload the twisting force when the internal twisting force of the round balance rope is too large, so as to prevent it from being twisted together due to excessive twisting force. However, few scholars have been involved in the study of hoisting system dynamics with friction constraint boundary. Therefore, the coupling dynamics of time-varying length hoisting rope and slack low-tension round balance rope are studied in this paper by considering their internal longitudinal-torsional coupling characteristics. The nonlinear dynamic behaviors of slack low-tension round balance rope are analyzed under excitation and boundary conditions by friction contact.

In this paper, flexible tensioned hoisting ropes on both sides of traction sheave are modeled based on variable-length finite element method. Dynamic model with friction constraint of round balance rope is established through absolute nodal coordinate formulation, the directional cosine matrix, Costello theory along with Coulomb's friction law. Then, the relationships between conveyances, tensioned hoisting ropes, flexible low-tension round balance rope and RBRSD are established through boundary constraint equation, and a nonlinear dynamic model coupling bilateral and unilateral constraint equations is obtained. Finally, using the unconditionally stable extended KDP generalized-α method, the dynamic behaviors of longitudinal-torsional-lateral round balance rope combined with hoisting rope with unbalanced factor are analyzed by numerical simulation.

The main novelties and contributions of our work are summarized as follows:

- In theory, a coupling dynamic model of rigid guide friction hoisting system is established. The longitudinal vibration of any point on the hoisting ropes and the four-dimensional (three-directional translation and one-directional rotation) vibrations of any point on the slack round balance rope are considered.
- Longitudinal-torsional-lateral dynamic model with friction constraint of round balance rope is established. Internal longitudinal-torsional coupling characteristics of round balance rope as well as unilateral constraint boundary among RBRSD and round balance rope are considered.
- Non-stationary responses of flexible low-tension round balance rope combined with flexible tensioned hoisting ropes are investigated considering excitation and complex coupling boundary.

Coupling Dynamics Model of Round Balance Rope and Hoisting Rope

In the multi-rope friction hoisting system is depicted in Fig. 1(a), where the number of hoisting ropes is usually more than 4, and the number of balance ropes is half of that of hoisting ropes. The hoisting rope is connected to conveyance through the tension-balanced device. Under the normal operating conditions of tension-balanced device,
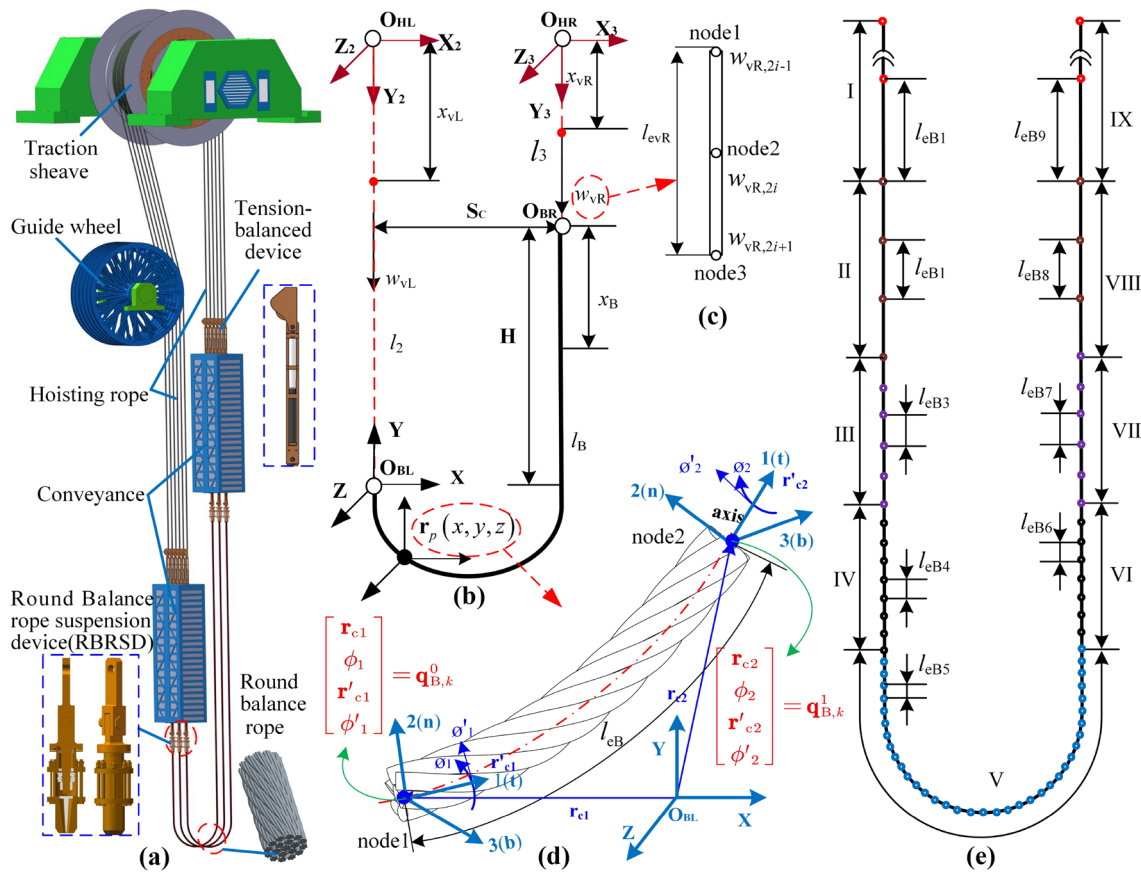
Fig. 1 **a** Three-dimensional model of friction hoisting system with round balance rope; **b** The reference coordinate systems of balance rope ($O_{BL}XYZ$), left hoisting rope ($O_{HL}X_2Y_2Z_2$) and right hoisting rope($O_{HR}X_3Y_3Z_3$); **c** Three-node rod element of hoisting rope;

d Two-node longitudinal-torsional-lateral coupled model of round balance rope; **e** Multi-segments non-equal-length element division method on round balance rope

the hoisting tension of each hoisting rope is basically the same. At this time, multiple hoisting ropes can be equivalent to single hoisting rope for dynamic modeling. Since, each round balance rope is suspended independently at the bottom of conveyance, multiple round balance ropes can also be equivalently established as the dynamic model of single round balance rope. This paper focuses on the coupling dynamic behavior of round balance rope and hoisting rope of friction hoisting system under normal operating conditions of tension-balanced device.

Several assumptions are made before deriving the dynamic model:

- The multi-rope friction hoisting system in this paper is simplified as single-rope friction hoisting system.
- The rigid guide of the friction hoisting system can constrain the in-plane, out-of-plane lateral displacement, and torsional displacement of conveyance. Therefore, only the longitudinal vibration of hoisting rope is considered.

- Due to the length of catenary section between traction sheave and guide wheel is short, it is ignored in order to simplify the dimension of the dynamic equation matrix.
- Ignoring the friction among the wires in the wire rope.
- The wire rope deforms evenly under force, and the cross section remains perpendicular to the centroid line during deformation.
- The steel wire rope for mining is sealed at both ends. In reality, the wire rope will not disperse during the operation of the hoist. Therefore, the rope material is an isotropic elastomer. The rope properties such as moment, mass, section area, Young's modulus [25] are assumed to be constant.

Physical description

The friction hoisting system, depicted in Fig. 1(a), is comprised of hoisting ropes, conveyances, balance ropes, round balance rope suspension device (RBRSD), guide wheel and traction sheave. Hoisting ropes are variable-length tension cable system, while round balance rope is a constant-length flexible low-tension cable system with time-varying curvature.

The constant-length round balance rope with time-varying boundaries and the variable-length cable system are coupled at the sheave, conveyances and RBRSD. The absolute coordinate system used in round balance rope, and the relative coordinate system used in left and right hoisting ropes are shown in Fig. 1(b). In this paper, the connecting point between the left conveyance and constant-length round balance rope is set as absolute coordinate frame $O_{BL}XYZ$. The reference coordinate frame $O_{HL}X_2Y_2Z_2$ and $O_{HR}X_3Y_3Z_3$ are established at the contact points between the traction sheave and left hoisting rope and right hoisting rope, respectively. O_{HL}, O_{BL}, O_{BR}, and O_{HR} are denoted as the connecting point between the round balance rope and left conveyance, contact point between the left hoisting rope and traction sheave, contact point between the right hoisting rope and traction sheave, and contact point between the round balance rope and right conveyance, respectively.

The coupling of the round balance rope friction hoisting system is mainly reflected in the complex coupling relationship of multiple objects at the connection boundary with bilateral constraints and unilateral constraints, the coupling of the longitudinal and torsional stiffness parameters of the wire rope, along with the nonlinear large deformation rigid-flexible coupling of slack rope.

Derivation of Governing Equations

Energy Equation of Hoisting Rope

The length of left and right hoisting ropes are $l_2(t)$ and $l_3(t)$, which are uniformly divided into n_{vL} and n_{vR} elements, respectively. The left and right hoisting ropes element length are $l_{evL}(t) = l_2(t)/n_{vL}$ and $l_{evR}(t) = l_3(t)/n_{vR}$, respectively. Variable-length finite element method is used to establish the dynamic model of hoisting ropes on both sides. Dynamic longitudinal displacement of hoisting ropes is discretized using a three-node rod element shown in Fig. 1(c). The dynamic longitudinal displacement of any point on left and right hoisting ropes are:

$$w_{vL}(x,t) = \mathbf{N}_{vL}\left(x, l_{evL}(t)\right)\mathbf{q}_{vL,i}(t), (i-1)l_{evL} \leqslant x \leqslant i \cdot l_{evL}$$
$$w_{vR}(x,t) = \mathbf{N}_{vR}\left(x, l_{evR}(t)\right)\mathbf{q}_{vR,i}(t), (i-1)l_{evR} \leqslant x \leqslant i \cdot l_{evR}$$

(1)

where $\mathbf{q}_{vL,i} = \left[w_{vL,i-1} \; w_{vL,i} \; w_{vL,i+1}\right]^T$ and $\mathbf{q}_{vR,i} = \left[w_{vR,i-1} \; w_{vR,i} \; w_{vR,i+1}\right]^T$ are dynamic longitudinal displacement vectors. $\mathbf{N}_{vL}$ and $\mathbf{N}_{vR}$ are the quadratic Lagrange interpolation element shape function of left and right hoisting ropes:

$$\mathbf{N}_{vL}\left(x, l_{evL}(t)\right) = \begin{bmatrix} 1 - 3\xi_{vL} + 2\xi_{vL}^2 \\ -4\left(\xi_{vL}^2 - \xi_{vL}\right) \\ 2\xi_{vL}^2 - \xi_{vL} \end{bmatrix}^T$$

$$\mathbf{N}_{vR}\left(x, l_{evR}(t)\right) = \begin{bmatrix} 1 - 3\xi_{vR} + 2\xi_{vR}^2 \\ -4\left(\xi_{vR}^2 - \xi_{vR}\right) \\ 2\xi_{vR}^2 - \xi_{vR} \end{bmatrix}^T$$

(2)

where $\xi_{vL}(x,t) = \frac{x}{l_{evL}} - i + 1$, $\xi_{vR}(x,t) = \frac{x}{l_{evR}} - i + 1$, $0 \leqslant \xi_{vL}, \xi_{vR} \leqslant 1$, $1 \leqslant i \leqslant n_{vL}, n_{vR}$.

The element kinetic energy of hoisting ropes and conveyances are:

$$E_{K,H} = \frac{1}{2}\rho_2 \sum_{i=1}^{n_{vL}} \int_{(i-1)\cdot l_{evL}}^{i\cdot l_{evL}} \left(\frac{Dw_{vL}}{Dt} + v_{vL}\right)^2 dx$$
$$+ \frac{1}{2}\rho_3 \sum_{i=1}^{n_{vR}} \int_{(i-1)\cdot l_{evR}}^{i\cdot l_{evR}} \left(\frac{Dw_{vR}}{Dt} + v_{vR}\right)^2 dx$$
$$+ \frac{1}{2}M_{CL}\left(\dot{q}_{CL} + v_{vL}\right)^2 + \frac{1}{2}M_{CR}\left(\dot{q}_{CR} + v_{vR}\right)^2$$

(3)

where the operator D/Dt is given by $D/Dt = \partial/\partial t + v(\partial/\partial x)$. ρ_2 and ρ_3 represent linear density of left and right hoisting ropes, respectively, where $\rho_2 = \rho_3$. M_{CL} and M_{CR} are mass of left and right conveyances. $\dot{q}_{CL}$ and $\dot{q}_{CR}$ are the first derivative of longitudinal displacements of left and right conveyances q_{CL} and q_{CR} with respect to time. v_{vL} and v_{vR} are velocities of left and right hoisting ropes and conveyances.

The strain energy $E_{U,H}$ in hoisting ropes is formulated as

$$E_{U,H} = \frac{1}{2}Q_{a2} \sum_{i=1}^{n_{vL}} \int_{(i-1)\cdot l_{evL}}^{i\cdot l_{evL}} \left(\varepsilon_{vL}\right)^2 dx$$
$$+ \frac{1}{2}Q_{a3} \sum_{i=1}^{n_{vR}} \int_{(i-1)\cdot l_{evR}}^{i\cdot l_{evR}} \left(\varepsilon_{vR}\right)^2 dx$$
$$+ \zeta_v Q_{a2} \sum_{i=1}^{n_{vL}} \int_{(i-1)\cdot l_{evL}}^{i\cdot l_{evL}} \dot{\varepsilon}_{vL}\delta\varepsilon_{vL} dx$$
$$+ \zeta_v Q_{a3} \sum_{i=1}^{n_{vR}} \int_{(i-1)\cdot l_{evR}}^{i\cdot l_{evR}} \int_{(i-1)\cdot l_{evR}}^{i\cdot l_{evR}} \dot{\varepsilon}_{vR}\delta\varepsilon_{vR} dx$$

(4)

where ζ_v is damping coefficient. Q_{a2} and Q_{a3}, as well as ε_{vL} and ε_{vR} are longitudinal stiffness coefficient and strain of left and right hoisting ropes, separately. $\dot{\varepsilon}_{vL}$ and $\dot{\varepsilon}_{vR}$ are the first derivative of ε_{vL} and ε_{vR} with respect to time.

$$\varepsilon_{vL} = \frac{\partial w_{vL}}{\partial x} = \mathbf{N}'_{vL}\mathbf{q}_{vL,i},$$
$$\varepsilon_{vR} = \frac{\partial w_{vR}}{\partial x} = \mathbf{N}'_{vR}\mathbf{q}_{vR,i},$$
$$\dot{\varepsilon}_{vL} = \dot{\mathbf{N}}'_{vL}\mathbf{q}_{vL,i} + \mathbf{N}'_{vL}\dot{\mathbf{q}}_{vL,i},$$
$$\dot{\varepsilon}_{vR} = \dot{\mathbf{N}}'_{vR}\mathbf{q}_{vR,i} + \mathbf{N}'_{vR}\dot{\mathbf{q}}_{vR,i}$$

(5)

where $\dot{\mathbf{q}}_{vL}$ and $\dot{\mathbf{q}}_{vR}$ are the first time derivative of longitudinal displacement vectors $\mathbf{q}_{vL}$ and $\mathbf{q}_{vR}$. $\mathbf{N}'_{vL}$, $\mathbf{N}'_{vR}$, $\dot{\mathbf{N}}'_{vL}$ and $\dot{\mathbf{N}}'_{vR}$ are shown in Appendix. The longitudinal strain of the hoisting rope is linearly related to the longitudinal dynamic displacement vector.

The virtual work of gravity on any element of hoisting ropes and conveyances are:

$$
\begin{aligned}
E_{W,H} = {} & \rho_2 \sum_{i=1}^{n_{vL}} \int_{(i-1)\cdot l_{evL}}^{i\cdot l_{evL}} f_{kg} \delta w_{vL} dx + M_{CL} f_{kg} q_{CL} \\
& + \rho_3 \sum_{i=1}^{n_{vR}} \int_{(i-1)\cdot l_{evR}}^{i\cdot l_{evR}} f_{kg} \delta w_{vR} dx + M_{CR} f_{kg} q_{CR}
\end{aligned}
\tag{6}
$$

where f_{kg} is gravity.

Energy Equation of Round Balance Rope

Round balance rope, depicted in Fig. 1(a), is always in a U-shaped bending state with time-varying curvature in the middle. In order to model the large deformation round balance rope with considering internal twisting force due to the action of its helical twisting structure and its own gravity, torsion deformable spatial beam and longitudinal-torsional coupling effect, which are based on absolute nodal coordinate formulation and Costello theory respectively, are used to establish longitudinal-torsional-lateral coupled model of round balance rope. The two-node longitudinal-torsional-lateral coupled model of round balance rope is shown in Fig. 1(d). For the convenience of writing, the proposed dynamic modeling method (longitudinal-torsional-lateral coupling spatial rope element with 16 degrees of freedom based on absolute nodal coordinate formulation, the directional cosine matrix, and Costello theory [26]) of the round balance rope is simplified as ANCF16LC.

In order to reduce the element number of round balance rope, multi-segments non-equal-length element division method is adopted. The middle large curved part (Part V) and the straight line part on both sides (Part I and Part IX) are connected with the middle transition section (Part II, Part III, Part IV, Part VI, Part VII, and Part VIII) as shown in Fig. 1(e). The total length of round balance rope is l_B, and it is divided into (n_{B1}, n_{B2}, n_{B3}, n_{B4}, n_{B5}, n_{B6}, n_{B7}, n_{B8}, and n_{B9}) elements in each part along the central axis, separately. The element length in each part is l_{eB1}, l_{eB2}, l_{eB3}, l_{eB4}, l_{eB5}, l_{eB6}, l_{eB7}, l_{eB8}, and l_{eB9}, respectively.

In the absolute coordinate system $O_{BL}XYZ$, $\mathbf{r}_c$ is global position vector of spatial round balance rope centerline, and $\mathbf{r}_c = [r_X \ r_Y \ r_Z]^T$. The unit tangent axis, the unit normal axis and the unit sub-normal axis at the point p on the center line of the round balance rope are defined as $\mathbf{t}(x)$, $\mathbf{n}(x)$ and $\mathbf{b}(x)$, respectively. $\mathbf{n}(x)$ and $\mathbf{b}(x)$ are orthogonal

unit vectors of point p in the local coordinate system, and $\mathbf{n} \times \mathbf{b} = \mathbf{t}$. Therefore, the directional cosine matrix from the local coordinate system to the global coordinate system is $[\mathbf{t} \ \mathbf{n} \ \mathbf{b}]$, and the position vector of any point p in the corresponding section of the beam is

$$
\mathbf{r}_p = \mathbf{r}_c + [\mathbf{t} \ \mathbf{n} \ \mathbf{b}][0 \ y \ z]^T \tag{7}
$$

where $[0, y, z]^T$ is the coordinate vector of point p in the local coordinate system. The tangent basis vector is defined as $\mathbf{t} = \mathbf{r}'_c / \sqrt{\mathbf{r}'^T_c \mathbf{r}'_c}$. $\mathbf{r}'_c$ is the slope vector, and $\mathbf{r}'_c = \frac{\partial \mathbf{r}_c}{\partial x} = [r'_X \ r'_Y \ r'_Z]^T$.

For convenience, the direction of the local coordinate system vector $[\mathbf{t} \ \mathbf{n} \ \mathbf{b}]$ is represented by 1-axis, 2-axis and 3-axis. Assuming that the inertial coordinate system is rotated by 3–2-1 parallel to the local coordinate system and the corresponding Euler angle is Tait-Brian angle [23], then the rotation matrix Θ can be expressed as

$$
\begin{aligned}
\Theta &= \begin{bmatrix} c_2 c_3 & c_2 s_3 & -s_2 \\ -c_1 s_3 + s_1 s_2 c_3 & c_1 c_3 + s_1 s_2 s_3 & s_1 c_2 \\ s_1 s_3 + c_1 s_2 c_3 & -s_1 c_3 + c_1 s_2 s_3 & c_1 c_2 \end{bmatrix} \\
&= [\mathbf{t} \ \mathbf{n} \ \mathbf{b}],
\end{aligned}
\tag{8}
$$

where $c_\alpha = \cos(\vartheta_\alpha)$, $s_\alpha = \sin(\vartheta_\alpha)$, $\alpha = 1, 2, 3$. ϑ_3, ϑ_2 and ϑ_1 represent the angle of rotation around the 3-axis, 2-axis and 1-axis, respectively. And

$$
\begin{aligned}
\cos(\vartheta_2) &= \frac{\sqrt{(r'_X)^2 + (r'_Y)^2}}{\sqrt{(r'_X)^2 + (r'_Y)^2 + (r'_Z)^2}}, \\
\sin(\vartheta_2) &= \frac{-r'_Z}{\sqrt{(r'_X)^2 + (r'_Y)^2 + (r'_Z)^2}}, \\
\cos(\vartheta_3) &= \frac{r'_X}{\sqrt{(r'_X)^2 + (r'_Y)^2}}, \\
\sin(\vartheta_3) &= \frac{r'_Y}{\sqrt{(r'_X)^2 + (r'_Y)^2}}
\end{aligned}
\tag{9}
$$

Thereby, $\mathbf{r}'_c$ can be used to replace ϑ_2 and ϑ_3 to reduce the number of degrees of freedom. Therefore, the generalized element vector $\mathbf{r}_B^p$ can be expressed as

$$
\begin{aligned}
\mathbf{r}_B^p(x,t) &= \begin{bmatrix} \mathbf{r}_c(x,t) \\ \phi(x,t) \end{bmatrix} = [r_X \ r_Y \ r_Z \ \phi]^T \\
&= \mathbf{N}_B(\xi_B) \cdot \mathbf{q}_{B,k}(t)
\end{aligned}
\tag{10}
$$

where $\mathbf{N}_B$ represents Hermite interpolation element shape function matrix of round balance rope, and $\xi_B = x/l_{eB}$. $\mathbf{r}_c$ is the translational degree of freedom in X, Y, Z directions

in the generalized element vector, ø is the torsional degree of freedom.

$$
\begin{aligned}
&\mathbf{r}_c(x,t) = \begin{bmatrix} r_X & r_Y & r_Z \end{bmatrix}^T = \mathbf{S}_t \cdot \mathbf{q}_{B,k}, \\
&\mathbf{r}'_c(x,t) = \begin{bmatrix} r'_X & r'_Y & r'_Z \end{bmatrix}^T = \mathbf{S}'_t \cdot \mathbf{q}_{B,k}, \\
&\phi(x,t) = \mathbf{S}_r \cdot \mathbf{q}_{B,k}, \\
&\phi'(x,t) = \mathbf{S}'_r \cdot \mathbf{q}_{B,k}
\end{aligned}
\tag{11}
$$

where $\mathbf{S}t$ and $\mathbf{S}r$ are translation and rotation interpolation sub-matrices. $\mathbf{q}_{B,k}$ is the k-th element coordinate vector, and $\mathbf{q}_{B,k} = \begin{bmatrix} \mathbf{q}_{B,k}^0 & \mathbf{q}_{B,k}^1 \end{bmatrix}^T$, where $\mathbf{q}_{B,k}^0$ and $\mathbf{q}_{B,k}^1$ represent two nodes of the element respectively. $\mathbf{q}_{B,k}^0 = \begin{bmatrix} \mathbf{r}_c(0,t) & \phi(0,t) & \mathbf{r}'_c(0,t) & \phi'(0,t) \end{bmatrix}^T$, and $\mathbf{q}_{B,k}^1 = \begin{bmatrix} \mathbf{r}_c(l_{eB},t) & \phi(l_{eB},t) & \mathbf{r}'_c(l_{eB},t) & \phi'(l_{eB},t) \end{bmatrix}^T$.

The element kinetic energy, viscoelastic strain energy, gravity virtual work of round balance rope:

$$
T_k = \frac{1}{2}\rho \int_0^{V_t} \frac{D}{Dt}\left(\mathbf{r}_c + \mathbf{n}y + \mathbf{b}z \right)^T \frac{D}{Dt}\left(\mathbf{r}_c + \mathbf{n}y + \mathbf{b}z \right) \mathrm{d}V
\tag{12}
$$

$$
\begin{aligned}
U_k = &\frac{1}{2}\int_0^{l_t} \left(\begin{array}{c} (Q_{a1}\varepsilon + Q_{b1}\tau)\varepsilon \\ +(Q_{c1}\varepsilon + Q_{d1}\tau)\tau \end{array} \right)\mathrm{d}x \\
&+ \frac{1}{2}EI \int_0^{l_t} \kappa^2 \mathrm{d}x + \zeta_B EI \int_0^{l_t} \dot{\kappa}\delta\kappa \mathrm{d}x \\
&+ \zeta_B \int_0^{l_t} \left(Q_{a1}\dot{\varepsilon}\delta\varepsilon + Q_{d1}\dot{\tau}\delta\tau \right)\mathrm{d}x \\
&+ \frac{1}{2}\zeta_B\left(Q_{b1} + Q_{c1} \right)\int_0^{l_t} \left(\dot{\tau}\delta\varepsilon + \dot{\varepsilon}\delta\tau \right)\mathrm{d}x
\end{aligned}
\tag{13}
$$

$$
\delta W_{ext,k} = \int_0^{l_t} \delta\left(\mathbf{r}_B^p \right)^T f_{kg} \mathrm{d}x
\tag{14}
$$

ζ_B is the damping coefficient of round balance rope. EI, Q_{a1} and Q_{d1} are bending, longitudinal and torsional stiffness coefficients, respectively. Q_{b1} and Q_{c1} are longitudinal-torsional coupling stiffness coefficients of round balance rope. ε, κ, and τ represent axial strain, bending curvature [27] and torsional curvature [28] of round balance rope:

$$
\begin{aligned}
&\varepsilon = \frac{1}{2}\left(\mathbf{r}'^T_c \mathbf{r}'_c - 1 \right), \\
&\kappa = \| \mathbf{r}'_c \times \mathbf{r}''_c \| / \| \mathbf{r}'_c \|^3, \\
&\tau = \mathbf{n}'^T \mathbf{b}
\end{aligned}
\tag{15}
$$

Moreover, $\dot{\varepsilon}$, $\dot{\kappa}$ and $\dot{\tau}$ are the first time derivative of ε, κ, and τ

$$
\dot{\varepsilon} = \frac{\partial\varepsilon}{\partial\mathbf{q}_{B,k}}\dot{\mathbf{q}}_{B,k}, \quad \dot{\kappa} = \frac{\partial\kappa}{\partial\mathbf{q}_{B,k}}\dot{\mathbf{q}}_{B,k}, \quad \dot{\tau} = \frac{\partial\tau}{\partial\mathbf{q}_{B,k}}\dot{\mathbf{q}}_{B,k}
\tag{16}
$$

where $\dot{\mathbf{q}}_B$ is the first time derivative of round balance rope coordinate vector $\mathbf{q}_B$. It can be noted from Eq. (15) that the axial strain, bending curvature and torsional curvature of the round balance rope are high-order nonlinear functions of round balance rope element coordinate vector, and they show strong nonlinear coupling with each other. Therefore, the axial strain, bending curvature and torsional curvature of round balance rope are strongly nonlinear strains.

Constraint Equation Between Balance Rope and Hoisting Ropes

The upper end of hoisting rope is connected with the traction sheave, and the lower end is connected with the hoisting conveyance, so the constraint equations $\Phi_{H,N}$ of left and right hoisting ropes is expanded as

$$
\begin{aligned}
&g_1 = q_{vL,1} - e^s(t) = 0, \\
&g_2 = q_{vL,dof2} - q_{CL} = 0, \\
&g_3 = q_{vR,1} - e^s(t) = 0, \\
&g_4 = q_{vR,dof3} - q_{CR} = 0
\end{aligned}
\tag{17}
$$

$e^s(t)$ represents the longitudinal deviation from traction sheave on hoisting rope at upper end.

The bilateral constraint equation $\Phi_{B,N}$ between round balance rope and RBRSD is expanded as:

$$
\begin{aligned}
&g_5 = q_{B,1} - x_L = 0, \\
&g_6 = q_{B,2} - q_{CL} - y_L = 0, \\
&g_7 = q_{B,3} - z_L = 0 \\
&g_8 = q_{B,dof1-7} - x_R = 0, \\
&g_9 = q_{B,dof1-6} - q_{CR} - y_R = 0, \\
&g_{10} = q_{B,dof1-5} - z_R = 0
\end{aligned}
\tag{18}
$$

x_L, y_L, z_L x_R, y_R, z_R are the horizontal, lateral and vertical coordinates of the left and right ends of round balance rope. dof1, dof2 and dof3 are total number of degrees of freedom of round balance rope, left and right hoisting ropes, respectively.

When the internal twisting force T_{ITF} of round balance rope is greater than the friction torque T_{FT} in RBRSD, the left and right ends of round balance rope begin to twist around the axis. When the internal twisting force T_{ITF} is less than the friction torque T_{FT}, the left and right ends of the round balance rope remain stationary and do not produce torsion displacement around the axis. Therefore, the torsion boundary of round balance rope around the axis is unilateral constraint boundary. Tangential displacement Φ_T of torsion constraint in RBRSD is expanded as:

$$\begin{cases} g_1' = \dot{q}_{B,4} = 0 \\ g_2' = \dot{q}_{B,dof1-4} = 0 \end{cases}, \quad |T_{ITF,i}| < T_{FT,i}, \ i = 1,2$$

$$\begin{cases} g_1' = \dot{q}_{B,4} \neq 0 \\ g_2' = \dot{q}_{B,dof1-4} \neq 0 \end{cases}, \quad |T_{ITF,i}| \geqslant T_{FT,i}, \ i = 1,2 \tag{19}$$

Dynamic Equation of Hoisting Rope and Balance Rope

From Eqs. (3), (4), (6), (12), (13), (14), (17), (18) and (19), the dynamic equation of hoisting ropes combined with round balance rope can be obtained:

$$\begin{cases} \mathbf{M}_{ass}(\mathbf{q}_{ass}) \cdot \ddot{\mathbf{q}}_{ass} + \mathbf{C}_{ass}(\mathbf{q}_{ass}) \cdot \dot{\mathbf{q}}_{ass} + \mathbf{F}_{ass}^{ex} \\ + \mathbf{Q}_{ass}(\mathbf{q}_{ass}) + \mathbf{W}_N^T \lambda_N + \mathbf{W}_T^T \lambda_T = 0 \\ \Phi_N = 0 \end{cases} \tag{20}$$

where $\mathbf{q}_{ass} = \begin{bmatrix} (\mathbf{q}_{vL})^T & (\mathbf{q}_R)^T & q_{CL} & q_{CR} & (\mathbf{q}_B)^T \end{bmatrix}^T$ is total generalized coordinate vector. For a flexible cable system consisting of N elements, the generalized coordinates of the system $\mathbf{q}$ and the generalized coordinates of the k-th element can be given by the Boolean mapping matrix [29] $\mathbf{B}$, and $\mathbf{q}_k = \mathbf{B}\mathbf{q}$. Therefore, $\mathbf{q}_{B,k} = \mathbf{B}^B \mathbf{q}_B$, $\mathbf{q}_{vL,i} = \mathbf{B}^H \mathbf{q}_{vL}$, $\mathbf{q}_{vR,i} = \mathbf{B}^H \mathbf{q}_{vR}$. $\mathbf{B}^B$ and $\mathbf{B}^H$ are Boolean mapping matrix of round balance rope and hoisting rope.

$\mathbf{M}_{ass}(\mathbf{q}_{ass})$ and $\mathbf{C}_{ass}(\mathbf{q}_{ass})$ are mass and damping matrices of friction hoisting system.

$$\mathbf{M}_{ass}(\mathbf{q}_{ass}) = \mathrm{diag}(\mathbf{M}_{vL}, \mathbf{M}_{vR}, M_{CL}, M_{CR}, \mathbf{M}_B(\mathbf{q}_B))$$
$$\mathbf{C}_{ass}(\mathbf{q}_{ass}) = \mathrm{diag}(\mathbf{C}_{vL}, \mathbf{C}_{vR}, 0, 0, \mathbf{C}_B(\mathbf{q}_B)) \tag{21}$$

$\mathbf{M}_B(\mathbf{q}_B)$, $\mathbf{M}_{vL}$ and $\mathbf{M}_{vR}$ are total mass matrices of balance rope and hoisting ropes:

$$\mathbf{M}_B(\mathbf{q}_B) = \sum_{k=1}^{n_B} (\mathbf{B}^B)^T \mathbf{M}_{eB}(\mathbf{q}_{B,k}) \mathbf{B}^B$$

$$\mathbf{M}_{eB}(\mathbf{q}_{B,k}) = \rho_1 l_{eB} \int_0^1 \mathbf{S}_t^T \mathbf{S}_t d\xi_B$$

$$+ J_m l_{eB} \int_0^1 \left(\left(\frac{\partial \mathbf{n}}{\partial \mathbf{q}_{B,k}}\right)^T \frac{\partial \mathbf{n}}{\partial \mathbf{q}_{B,k}} + \left(\frac{\partial \mathbf{b}}{\partial \mathbf{q}_{B,k}}\right)^T \frac{\partial \mathbf{b}}{\partial \mathbf{q}_{B,k}} \right) d\xi_B \tag{22}$$

where $J_m = \rho_1 \int_{A_1} y^2 dA = \rho_1 \int_{A_1} z^2 dA$ is the rotational inertia of round balance rope.

$\mathbf{C}_B(\mathbf{q}_B)$, $\mathbf{C}_{vL}$ and $\mathbf{C}_{vR}$ are total damping matrices of balance rope and hoisting ropes:

$$\mathbf{C}_B(\mathbf{q}_B) = \sum_{k=1}^{n_B} (\mathbf{B}^B)^T \mathbf{C}_{eB}(\mathbf{q}_{B,k}) \mathbf{B}^B$$

$$\mathbf{C}_{eB}(\mathbf{q}_{B,k}) = \zeta_B l_{eB} \int_0^1 \begin{pmatrix} Q_{a1}\left(\frac{\partial \varepsilon}{\partial \mathbf{q}_{B,k}}\right)^T \frac{\partial \varepsilon}{\partial \mathbf{q}_{B,k}} \\ + Q_{d1}\left(\frac{\partial \tau}{\partial \mathbf{q}_{B,k}}\right)^T \frac{\partial \tau}{\partial \mathbf{q}_{B,k}} \\ + EI\left(\frac{\partial \kappa}{\partial \mathbf{q}_{B,k}}\right)^T \frac{\partial \kappa}{\partial \mathbf{q}_{B,k}} \end{pmatrix} d\xi_B$$

$$+ \frac{\zeta_B l_{eB}}{2}(Q_{b1} + Q_{c1}) \int_0^1 \begin{pmatrix} \left(\frac{\partial \tau}{\partial \mathbf{q}_{B,k}}\right)^T \frac{\partial \varepsilon}{\partial \mathbf{q}_{B,k}} \\ + \left(\frac{\partial \varepsilon}{\partial \mathbf{q}_{B,k}}\right)^T \frac{\partial \tau}{\partial \mathbf{q}_{B,k}} \end{pmatrix} d\xi_B \tag{23}$$

$\mathbf{Q}_{ass}(\mathbf{q}_{ass})$ and $\mathbf{F}_{ass}^{ex}$ are vectors of total elastic force and generalized external force of friction hoisting system.

$$\mathbf{Q}_{ass}(\mathbf{q}_{ass}) = \begin{bmatrix} \mathbf{K}_{vL} \cdot \mathbf{q}_{vL} \\ \mathbf{K}_{vR} \cdot \mathbf{q}_{vR} \\ 0 \\ 0 \\ \mathbf{Q}_B(\mathbf{q}_B) \end{bmatrix}, \mathbf{F}_{ass}^{ex} = \begin{bmatrix} \mathbf{F}_{vL}^{ex} \\ \mathbf{F}_{vR}^{ex} \\ F_{CL}^{ex} \\ F_{CR}^{ex} \\ \mathbf{F}_B^{ex} \end{bmatrix} \tag{24}$$

$\mathbf{Q}_B(\mathbf{q}_B)$ is elastic force vector of round balance rope.

$$\mathbf{Q}_B = \sum_{k=1}^{n_B} (\mathbf{B}^B)^T \mathbf{Q}_{eB}$$

$$\mathbf{Q}_{eB} = l_{eB} \int_0^1 \left(Q_{a1}\frac{\varepsilon\partial\varepsilon}{\partial\mathbf{q}_{B,k}} + Q_{d1}\frac{\tau\partial\tau}{\partial\mathbf{q}_{B,k}} + EI\frac{\kappa\partial\kappa}{\partial\mathbf{q}_{B,k}} \right)^T d\xi_B \tag{25}$$

$$+ \frac{l_{eB}}{2}(Q_{b1} + Q_{c1}) \int_0^1 \left(\frac{\tau\partial\varepsilon}{\partial\mathbf{q}_{B,k}} + \frac{\varepsilon\partial\tau}{\partial\mathbf{q}_{B,k}} \right)^T d\xi_B$$

$\mathbf{K}_{vL}$ and $\mathbf{K}_{vR}$ are total stiffness matrices of left and right hoisting ropes.

$\mathbf{F}_B^{ex}$, $\mathbf{F}_{vL}^{ex}$, $\mathbf{F}_{vR}^{ex}$, F_{CL}^{ex} and F_{CR}^{ex} are generalized external force vectors of round balance rope, hoisting ropes and conveyances. Φ_N denotes the bilateral constraint equation, and $\Phi_N = \begin{bmatrix} \Phi_{H,N} & \Phi_{B,N} \end{bmatrix}^T$.

$\mathbf{W}_N$ is the first-order partial derivative of the coordinate of bilateral constraints, and $\mathbf{W}_T$ is the vector of tangential force direction.

$$\mathbf{W}_N = \partial\Phi_N/\partial\mathbf{q}_B$$
$$\mathbf{W}_T = \partial\Phi_T/\partial\mathbf{q}_B \tag{26}$$

λ_N is Lagrange multipliers corresponding to the bilateral constraints. λ_T is the friction force of torsion constraint joint.

Using this projection function [30], combining Eqs. (20) with (19),we can yield

$$\begin{cases} \mathbf{M}_{\text{ass}}(\mathbf{q}_{\text{ass}}) \cdot \ddot{\mathbf{q}}_{\text{ass}} + \mathbf{C}_{\text{ass}}(\mathbf{q}_{\text{ass}}) \cdot \dot{\mathbf{q}}_{\text{ass}} + \mathbf{F}_{\text{ass}}^{\text{ex}} \\ + \mathbf{Q}_{\text{ass}}(\mathbf{q}_{\text{ass}}) + \mathbf{W}_{\text{N}}^{\text{T}} \lambda_{\text{N}} + \mathbf{W}_{\text{T}}^{\text{T}} \lambda_{\text{T}} = 0 \\ \mathbf{\Phi}_{\text{N}} = 0 \\ \lambda_{\text{T}} - \text{proj}_{C_{\text{T}}(T_{\text{m}})}(\lambda_{\text{T}} - \mathbf{W}_{\text{T}} \dot{\mathbf{q}}_{\text{ass}}) = 0 \end{cases} \quad (27)$$

In Eq. (27) the convex set C_{T} is

$$C_{\text{T}}(T_{\text{m}}) = \{x \in R | x \leqslant \mu |T_{\text{m}}|\} \quad (28)$$

T_{m} represents the torque force generated by the pressure at the RBRSD with round balance rope. μ is friction coefficient.

From Eqs. (22), (23) and (25), it can be noted that mass matrix, damping matrix and elastic force vector of the round balance rope are all high-order nonlinear functions of element coordinate vector, which are highly coupled, and their explicit integral expressions cannot be obtained. Therefore, Gauss–Legendre [31] polynomial is used to integrate the mass matrix, damping matrix and elastic force vector of round balance rope.

Equation (27) is nonlinear differential algebraic equations containing bilateral and unilateral constraint equations. It is impossible to reduce the unilateral constraint equations by simple reduction method. The extended KDP [32] generalized-α method in the literature [19] can be used to iteratively solve the nonlinear differential algebraic equations.

Application in Round Balance Rope Coupled With Hoisting Rope

In this section, the physical parameters of round balance rope and hoisting ropes used in simulation are shown in Table 1. And the physical parameters come from a mine in China. The hoisting ropes on both sides are divided into ten elements, and each hoisting rope has 22 degrees of freedom. v_{max}, a_{max} and t_{max} represent the maximum running speed, maximum acceleration and simulation time of the conveyance in the simulation. H and S_c represent the height difference and horizontal distance between the conveyances on both sides.

In order to reduce the element number of round balance rope, multi-segments non-equal-length element division method [33] is used as shown in Fig. 1(e). The division parameters of round balance rope of the multi-segment non-equal-length element are shown in Table 2, and 421 elements are discretized. If the equal-length element division method is used, 4832 elements will be generated. Compared with the equal-length element division method, the element number of multi-segment non-equal-length element division method is decreased by 91.3%. The dimension (degree of freedom) of round balance rope dynamic equation matrix is reduced by 35,288. That is to say, the multi-segment non-equal-length element division method can effectively reduce the number of elements of the dynamic system and reduce the dimension of the dynamic equation matrix.

Validation of the Theoretical Model of ANCF16LC

The verification of the ANCF16LC theoretical model can be divided into the verification of lateral-longitudinal rigid-flexible coupling large displacement of the balance rope and

Table 1 Physical parameters used in simulation

Parameter	Value	Parameter	Value	Parameter	Value
Q_{a1}, Q_{a2}, Q_{a3}	$1.097 \cdot 10^8$ N	EI	52.12 N·m^2	l_3	10 m
Q_{b1}	$2.371 \cdot 10^5$ N·m	$M_{\text{CL}}, M_{\text{CR}}$	10,000 kg	l_B	966.4 m
Q_{c1}	$2.301 \cdot 10^5$ N·m	R	2.5 m	H	899.2 m
Q_{d1}	$2.751 \cdot 10^3$ Nm^2	S_c	2.5 m	v_{max}	6 m/s
ρ_1, ρ_2, ρ_3	6.42 kg/m	l_2	910 m	a_{max}	0.75 m/s2

Table 2 Element division parameters of round balance rope

Section name	Section length	Element number	Element length	Total DOFs
Part I, Part IX	6.4 m, 905.6 m	2, 283	3.2 m	3376
Part II, Part VIII	6.4 m	4	1.6 m	
Part III, Part VII	6.4 m	8	0.8 m	
Part IV, Part VI	6.4 m	16	0.4 m	
Part V	16 m	80	0.2 m	

that of the longitudinal-torsional coupling vibration. That is, the correctness of the ANCF16LC model is verified by comparing the in-plane lateral-longitudinal coupling with the ANCF and the dynamic response of the longitudinal-torsional coupling based on the finite element method (FEMLC) which is proposed in literature [12].

During the movement of the hoisting system, coal powder may increase the frictional resistance coefficient μ of the RBRSD. Therefore, we will study the coupling dynamic behavior characteristics of hoisting rope and round balance rope in the following process when the frictional resistance coefficient $\mu = 0$ and $\mu \neq 0$. With the parameters in Tables 1 and 2 used, and the initial shape local area amplification diagrams based on ANCF16LC and ANCF modeling methods are depicted in Fig. 2, when the torque force $T_m = 40 \text{N·m}$. The red solid line, black dotted line and magenta dotted line represent the initial equilibrium position curves of ANCF16LC at $\mu = 0.1$, $\mu = 0$ and ANCF, respectively. Figure 2(a), (b), (c) and (d) represent three-dimensional configuration of round balance rope, and its projection curves on X–Y plane, Z-Y plane, and Φ-Y plane in the initial states.

From Fig. 2(a) and (b), it can be seen that the black dotted and magenta dashed lines completely coincide, that is, the twisting force in the round balance rope with ANCF16LC at $\mu = 0$ is released by the balance rope suspension device,
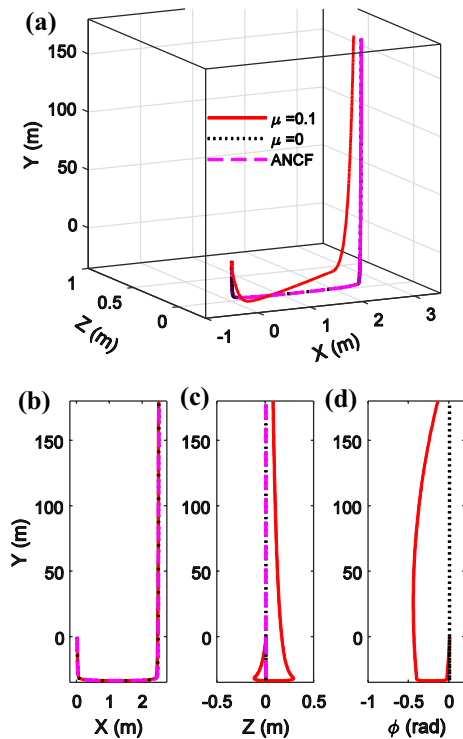
thus the same plane configuration as ANCF can be obtained. Since the coupled stiffness coefficients of round balance rope is not zero, the longitudinal deformation of round balance rope will cause torsional deformation of round balance rope shown in Fig. 2(d) when $\mu = 0.1$, which will drive the torsion of round balance rope, and then generate out-of-plane lateral displacement shown in Fig. 2(c). It is noted that the maximum torsional angle of balance rope due to the longitudinal-torsional coupling effect appears at the balance rope loop in the longer side of the balance rope when $\mu \neq 0$. Due to the effect of torsional force and torsion angle, the maximum out-of-plane lateral displacement of balance rope also appears at the same area.

With the twisting force inside the round balance rope neglected, that is, $\mu = 0$, the first two longitudinal natural frequencies of hoisting ropes and round balance rope are shown in Fig. 3(a) and (b). The boundary of hoisting system is set to fixed boundary without any excitation, and the equilibrium state ē of the hoisting system is solved by Matlab under different height difference. The previous equilibrium state ē is brought into the Matlab to solve the natural frequency and mode of the hoisting system. Beam188 element is used to solve the natural frequency of round balance rope and hoisting ropes in ANSYS. The black dash dot line and red dashed line represent the longitudinal natural frequency curve of the round balance rope obtained by ANCF16LC and ANSYS, respectively. H represents the height difference between the conveyances on both sides. In order to facilitate the study of the large deformation dynamic response of the balance rope of the hoisting system under longitudinal excitation, the excitation frequency curve is drawn together with the natural frequency. In Fig. 3(a), the blue solid line represents curve of excitation frequency ω at the traction sheave. Longitudinal excitation function $e^s(t)$ is defined as
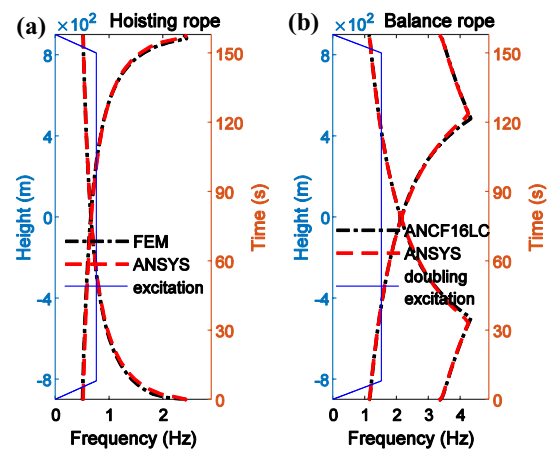

Fig. 2 **a** Three-dimensional configuration of round balance rope in initial state, **b** its projection on the X–Y plane, **c** its projection on the Z-Y plane and **d** its projection on the Φ-Y plane

Fig. 3 First 2 longitudinal natural frequencies of **a** hoisting rope and **b** balance rope

$e^s(t) = A_0 \cdot \sin(\omega \cdot t)$, where $\omega = k \cdot v/R$. A_0, R and v represent the excitation amplitude, radius of traction sheave, and velocity, respectively. k represents a multiple relationship. The blue solid line represents curve of double excitation frequency 2ω in Fig. 3(b).

In order to verify the longitudinal-torsional coupling ability of ANCF16LC, the dynamic response of ANCF16LC is compared with that of FEMLC. Because FEMLC can only establish the coupling vibration model of small deformation of the tensioned rope system, it is impossible to establish the dynamic model of the slack low-tension rope with large displacement and large deformation. Therefore, the tensioned rope system shown in Fig. 4(a) is used for comparative analysis. Among them, the rope length $l_m = 50$ m, the mass weight $M_c = 10{,}000$ kg, elastic stiffness, torsional stiffness and coupling stiffness coefficient are the same as those in Table 1, the excitation frequency $\omega_e = 1.8$ Hz, and the excitation amplitude $A_0 = 0.01$ m. The longitudinal-torsional coupling dynamic response of wire rope obtained by two methods is portrayed in Fig. 4(b) and (c), in which blue solid line and the red dotted line represent the vibration obtained by the FEMLC and ANCF16LC methods, respectively. Under longitudinal excitation, the wire rope system produces longitudinal resonance (beat vibration) as shown in Fig. 4(b)

due to gravity, and longitudinal vibration causes torsional vibration as depicted in Fig. 4(c). It can be demonstrated that the curves obtained by the two methods are well matched. Therefore, the dynamic modeling method of ANCF16LC is correct in terms of longitudinal-torsional coupling.

The ANCF16LC, a two-node element with 16 degrees of freedom per element, can describe the geometrical nonlinearity when the medium is undergoing large displacement and rotation. It can be used for the tensioned rope system, and also for the large deformation dynamic modeling of the slack low-tension system. The FEMLC, a three-node element with 6 degrees of freedom per element, is only suitable for the tensioned rope system. It is difficult to describe the geometrical nonlinearity of the medium under large displacement and large rotation.

To sum up, lateral-longitudinal-torsional coupling dynamic model (ANCF16LC) is compared and validated in terms of space configuration of ANCF, as well as the longitudinal-torsional coupling dynamic response of FEMLC.

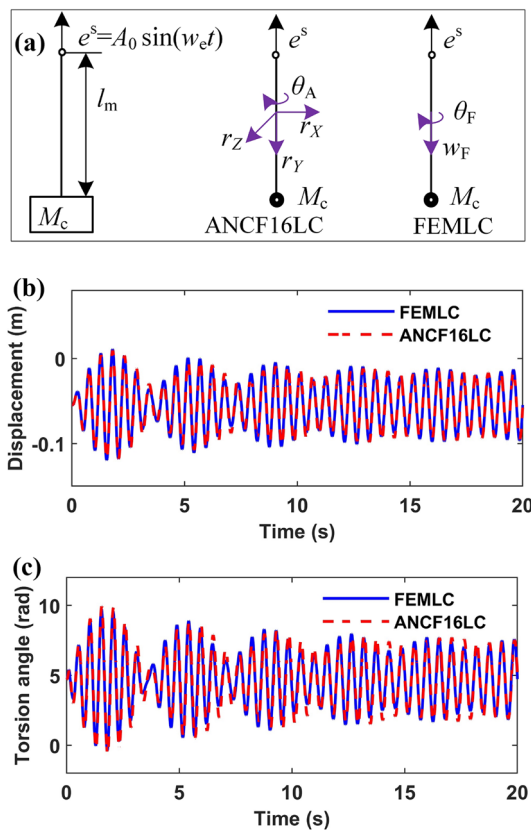## Dynamic Characteristics of Longitudinal-Torsional-Lateral Round Balance Rope Coupled With Hoisting Ropes

Since the extrusion and wear of the hoisting rope on the traction sheave during long-term operation, the rope groove in contact with the hoisting rope becomes an irregular circle with undulating surface. Therefore, the traction sheave will generate simple harmonic excitation during the operation of the hoisting system. It is assumed that the double frequency excitation is produced due to the wear of the traction sheave rope groove, that is, $k = 2$. The dynamic responses at the left and right conveyances are shown in Fig. 5 with parameters in Tables 1 and 2 adopted. The results show that the left conveyance and right conveyance resonate in the region near 110 s and near 60 s, respectively.

The torsional angular velocities of the left and right ends of the round balance rope rotating around the Y-axis are shown in Fig. 6(a) and (b). The plus and minus sign indicates the direction of rotation, where the former indicates a rightward rotation, and the latter indicates a leftward rotation. It can be seen from two diagrams that the torsional angular velocities at the left and right ends resonates in the area near 60 s and 110 s, and changes dramatically. This is because the longitudinal resonance of the hoisting rope will be transmitted to the round balance rope, once it occurs. Then, the longitudinal vibration of the round balance rope causes the left and right ends to rotate and oscillate greatly around the Y-axis under the action of the longitudinal-torsional coupling stiffness of the round balance rope.

The maximum lateral displacements of the round balance rope with time on the X–Y plane and Z-Y plane are depicted
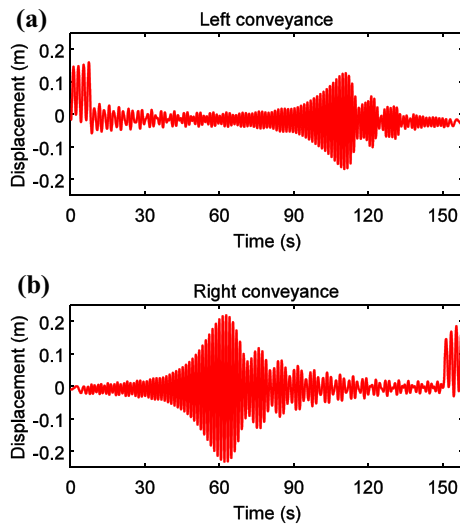

Fig. 4 **a** Longitudinal-torsional coupling comparison diagram; **b** Longitudinal displacements and **c** torsion angle of end of wire rope

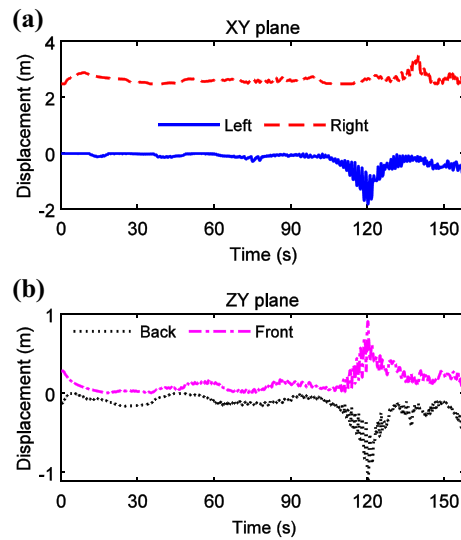**Fig. 5** Longitudinal dynamic displacements of left and right conveyances

Fig. 7 Maximum lateral displacements of the round balance rope on the **a** X–Y plane and **b** Z-Y plane
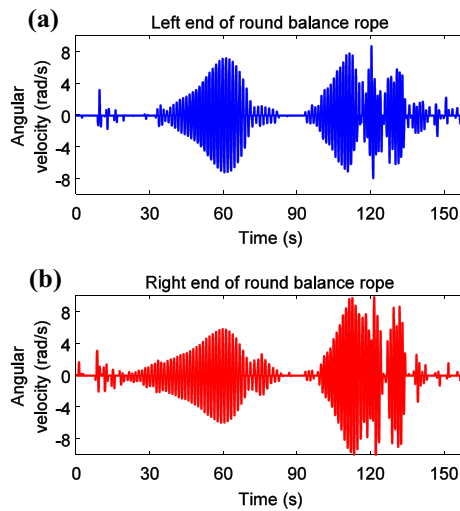

Fig. 6 Torsional angular velocities of the **a** left and **b** right ends of round balance rope
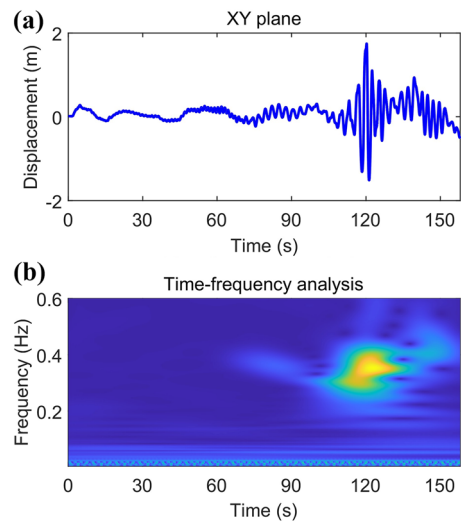

Fig. 8 **a** Lateral displacement at left observation point on the X–Y plane, and **b** its corresponding time–frequency analysis map

in Fig. 7(a) and (b) under the coupling of round balance rope combined with hoisting ropes. In the projection of the X–Y plane depicted in Fig. 7 (a), the blue solid line represents the displacement curve in the left direction of X-axis, and the red dashed line represents the displacement curve in the right direction of X-axis. In the projection of the Z-Y plane shown in Fig. 7(b), the black dotted line represents the displacement curve in the back direction of Z-axis, and the magenta dash-dot line represents the displacement curve in the front direction of Z-axis. It can be seen from Fig. 7 that the round balance rope performs a large displacement swing around 120 s.

Two observation points are set at the horizontal position 20 m below the left conveyance in the initial state to observe the lateral displacement of both sides of round balance rope. The lateral displacement at the left observation point on the X–Y plane is shown in Fig. 8(a), and its corresponding time–frequency analysis map is shown in Fig. 8(b). The time–frequency analysis in Fig. 8(b) shows that the highlight area near the 120 s region is the time period with large vibration energy of the balance rope. At this time, the transverse vibration frequency of the balance rope is about 0.38 Hz, which is much higher than its

own first-order lateral natural frequency, and the vibration amplitude is large.

The projection of spatial configurations of round balance rope are depicted in Fig. 9(a) and (b) at 117 s and 120 s on the X–Y plane and Z-Y plane. The blue solid line and red dash-dot line represent the in-plane and out-of-plane projection of round balance rope. It is noted that the in-plane and out-of-plane lateral deformations of the round balance rope are relatively severe at 117 s and 120 s. Besides, the maximum in-plane lateral displacement of the round balance rope reaches about 2 m, and the maximum out-of-plane lateral displacement exceeds 1 m at 120 s. Because of large dynamic displacement and narrow installation spacing of round balance rope is with about 0.6 m, two adjacent round balance ropes are likely to collide, twine and kink together, which brings hidden danger to the mine hoisting system.

The in-plane and out-of-plane phase diagrams at the left and right observation points are shown in Fig. 10. In the vicinity of 120 s, the phase diagram of the left round balance rope is intended to be far away from the origin. That is to say, the round balance rope is in danger of instability near 120 s.
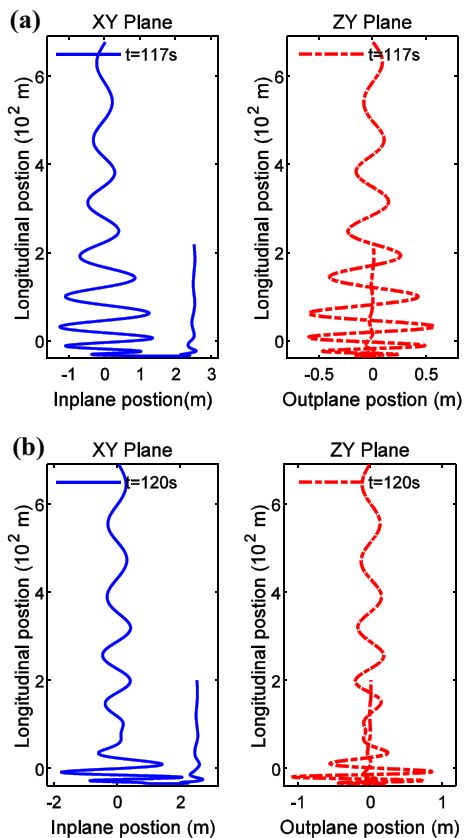
Fig. 10 Phase diagram of left and right observation points of round balance rope

Fig. 9 Projection of spatial configurations of round balance rope under different time

There are several main reasons about the in-plane and out-of-plane large displacements of round balance rope:

(1) The hoisting ropes resonate under the action of longitudinal excitation at the upper end, resulting in large longitudinal vibration amplitude, which is transmitted to the round balance rope through the hoisting conveyances. Therefore, the left and right ends of round balance rope are subjected to longitudinal excitation with relatively large amplitude.

(2) From the formula of bending curvature and axial strain, they are highly coupled. The round balance rope is a long-distance low-tension rope, and its axial deformation will be transformed into bending deformation at the bending part in the round balance rope loop.

(3) The running speed of the hoisting system is not very high, and the transient resonance in the hoisting system exists for a long time.

(4) There is an intersection between the doubling longitudinal excitation frequency curve and the longitudinal natural frequency curve of the round balance rope as shown in Fig. 3(b). And the intersection frequency point is near 120 s, which is consistent with the time period when the round balance rope undergoes large deformation.

(5) The intersection of the doubling longitudinal excitation frequency curve and the longitudinal natural frequency curve of the round balance rope should be after the intersection of the natural frequency curve of hoisting rope and the excitation frequency curve, as shown in Fig. 3(a) and (b). Therefore, the significant in-plane

and out-of-plane displacements of the round balance rope appear only in the region near 120 s, but not in the region near 45 s.

(6) The twisting force inside round balance rope makes the bottom of the round balance rope produce a spatial out-of-plane deformation in a buckling shape. Two points on the left and right side round balance rope on the same horizontal plane are taken for force analysis. The force diagrams of point A and point B at the balance rope loop are illustrated in Fig. 11 (a).

According to the spatial form of the balance rope, the direction of F_{a1} is the tangent direction inclined to the rear and lower part, and the direction of F_{b1} is the tangent direction inclined to the front and upper part.

The projection of F_{a1} in X-, Y-, Z- axis are $F_{a1,x}$, $F_{a1,y}$, $F_{a1,z}$, and the projection of F_{b1} on X-, Y-, Z- axis are $F_{b1,x}$, $F_{b1,y}$, $F_{b1,z}$. The projection resultant force of left and right side round balance rope on X-, Y-, and Z- axes are shown in Fig. 11 (b). $F_{a,X}$, $F_{a,Y}$, $F_{a,Z}$, $F_{b,X}$, $F_{b,Y}$, and $F_{b,Z}$ are

$$\begin{cases} F_{a,X} = \sum_{i=1}^{n_a} F_{a1,x} \\ F_{a,Y} = \sum_{i=1}^{n_a} F_{a1,y} \\ F_{a,Z} = \sum_{i=1}^{n_a} F_{a1,z} \end{cases}, \begin{cases} F_{b,X} = \sum_{i=1}^{n_b} F_{b1,x} \\ F_{b,Y} = \sum_{i=1}^{n_b} F_{b1,y} \\ F_{b,Z} = \sum_{i=1}^{n_b} F_{b1,z} \end{cases} \quad (29)$$

$F_{a,X}$ and $F_{b,X}$ are in the same direction, and will form a horizontal left (right) force F_X, as shown in Fig. 11(b). The balance rope loop at the bottom of round balance rope is driven by the horizontal force F_X, causing the round balance rope to sway in-plane. The directions of $F_{a,Z}$ and $F_{b,Z}$ are opposite. When $F_{a,Z} \neq F_{b,Z} \neq 0$, $F_{a,Z}$ and $F_{b,Z}$ will form

a torsional moment M_z in the counterclockwise (clockwise) direction as shown in Fig. 11(b). The size and direction of M_z depend on the longitudinal and torsional coupling stiffness coefficient of the wire rope, the friction resistance coefficient of the RBRSD and the longitudinal length of the round balance rope. Out-of-plane swing occurs on the balance rope loop of round balance rope under the action of torsional moment M_z. When there is no external excitation, the direction of M_z does not change, then the swing of the left or right side round balance rope outside the plane only swings in the positive or negative area of the Z axis, and there will be no jump in the positive and negative areas.

When the round balance rope suffers longitudinal resonance, the lateral vibration response at round balance rope loop changes from low-frequency oscillation with small amplitude to high-frequency vibration with large amplitude from Fig. 8. Large amplitude longitudinal vibration produces large amplitude torsional vibration under the action of longitudinal-torsional coupling stiffness. The direction of resultant moment M_z changes with the torsion of round balance rope, which drives the round balance rope to swing out-of-plane. With the increase of the in-plane and out-of-plane lateral displacements of round balance rope, the nonlinear dynamic phenomenon occurs.

In order to avoid unsafe situations such as collision and winding of round balance rope, we need to pour attention into large in-plane and out-of-plane dynamic deformation amplitude of round balance rope. By regularly checking the wear of the traction sheave and repairing the traction sheave, the system can be improved from the excitation source to avoid the occurrence of resonance. Avoid the intersection of doubling frequency of excitation and the longitudinal natural frequency of round balance rope, that is, avoid the longitudinal resonance of round balance rope. Reduce the longitudinal and torsional coupling stiffness coefficient of round balance rope and the friction resistance coefficient of RBRSD, thereby reducing the torsional moment M_z, in order to reduce the out-of-plane vibration displacement of round balance rope.

Conclusion

In this study, a coupling modeling method of variable-length hoisting ropes as well as variable-curvature torsion deformable spatial balance rope is proposed in ultra-kilometer deep shaft friction hoisting system. The relationships between rigid body, such as traction sheave and conveyances, and flexible body, such as, tensioned hoisting ropes and flexible low-tension round balance rope, are established through boundary constraint equation. Dynamic characteristics of longitudinal-torsional-lateral round balance rope coupled with hoisting ropes are revealed by solving the nonlinear differential algebraic
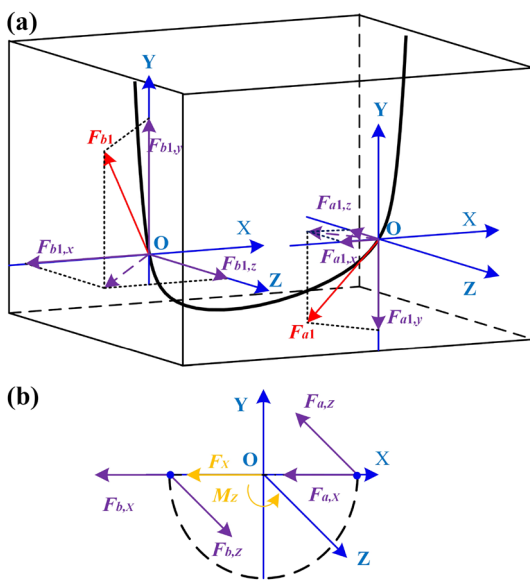

Fig. 11 Force diagram of any point at the round balance rope loop

equations, which contains bilateral and unilateral constraint equations, using the extended KDP generalized-α method.

On the basis of the numerical results displayed in this paper, it can be seen that the multi-body longitudinal-torsional-lateral coupled dynamic modeling method proposed in this paper is feasible, and multi-segments non-equal-length element division method can effectively reduce the dimension of the dynamic equation matrix. Under the given conditions in this paper, the round balance rope with friction constraint boundary has undergone severe large in-plane and out-of-plane displacement and deformation. It has been concluded that the main reasons leading to large in-plane and out-of-plane displacement are longitudinal resonance of hoisting ropes, high coupling of axial strain with bending and torsional curvature in flexible low-tension round balance rope, a long time transient resonance, intersection between the doubling longitudinal excitation frequency and longitudinal natural frequency of round balance rope, and torsional moment M_z from twisting force inside round balance rope. In order to avoid unsafe situations such as collision and winding of round balance rope and improve the safety of mine hoisting system, it is necessary to pour attention into large in-plane and out-of-plane deformation dynamic amplitude of round balance rope.

In this study, multiple hoisting ropes are equivalent to single hoisting rope for dynamic modeling under normal operating conditions of tension-balanced device. Only when the tension-balanced device fails, the tension difference is distinct between the hoisting ropes, and the dynamic model of all hoisting ropes needs to be established. In future work, we will further consider the coupling dynamic behavior of the round balance rope and the hoisting rope in the friction hoisting system, such as the abnormal condition of the tension-balanced device. Furthermore, the hysteresis and internal damping dissipation, caused by the twisting and untwisting of the wire rope, will be further studied in future work.

Appendix

$$
\begin{aligned}
\dot{\mathbf{N}}_{vL} &= \dot{\xi}_{vL}\left[\left(-3+4\xi_{vL}\right)\ -4\left(2\xi_{vL}-1\right)\ \left(4\xi_{vL}-1\right)\right] \\
\ddot{\mathbf{N}}_{vL} &= \ddot{\xi}_{vL}\left[\left(-3+4\xi_{vL}\right)\ -4\left(2\xi_{vL}-1\right)\ \left(4\xi_{vL}-1\right)\right] \\
&\quad +4\dot{\xi}_{vL}^2\left[1\ -2\ 1\right] \\
\dot{\mathbf{N}}'_{vL} &= \dot{\xi}'_{vL}\left[\left(-3+4\xi_{vL}\right)\ -4\left(2\xi_{vL}-1\right)\ \left(4\xi_{vL}-1\right)\right] \\
&\quad +4\dot{\xi}_{vL}/l_{evL}\left[1\ -2\ 1\right] \\
\mathbf{N}'_{vL} &= 1/l_{evL}\left[\left(-3+4\xi_{vL}\right)\ -4\left(2\xi_{vL}-1\right)\ \left(4\xi_{vL}-1\right)\right] \\
\mathbf{N}''_{vL} &= \frac{4}{l_{evL}^2}\left[1\ -2\ 1\right] \\
\dot{\xi}_{vL} &= -v_{evL}\cdot x/l_{evL}^2 \\
\dot{\xi}'_{vL} &= -v_{evL}/l_{evL}^2 \\
\ddot{\xi}_{vL} &= -a_{evL}\cdot x/l_{evL}^2\ +2v_{evL}^2\cdot x/l_{evL}^3
\end{aligned}
\tag{30}
$$

The shape function matrix $\mathbf{N}_B$

$$
\mathbf{N}_B = \left[\ N_{B,1}\ N_{B,2}\ N_{B,3}\ N_{B,4}\ \right] \otimes \mathbf{I}_4
\tag{31}
$$

$\mathbf{I}_4$ is a 4-order identity matrix, and

$$
\begin{aligned}
N_{B,1}(\xi_B) &= 1 - 3\xi_B^2 + 2\xi_B^3, \\
N_{B,2}(\xi_B) &= l_{eB}\left(\xi_B - 2\xi_B^2 + \xi_B^3\right), \\
N_{B,3}(\xi_B) &= 3\xi_B^2 - 2\xi_B^3, \\
N_{B,4}(\xi_B) &= l_{eB}\left(-\xi_B^2 + \xi_B^3\right)
\end{aligned}
$$

$\mathbf{S}t$ and $\mathbf{S}r$ are translation and rotation interpolation sub-matrices.

$$
\mathbf{N}_B = \begin{bmatrix}\mathbf{S}_t \\ \mathbf{S}_r\end{bmatrix}, \mathbf{S}_t = \mathbf{N}_B(1:3,:), \mathbf{S}_r = \mathbf{N}_B(4,:).
$$

$\mathbf{N}'_B$ and $\mathbf{N}''_B$ represents first-order and second-order spatial slope of Eq. (31)

$$
\begin{aligned}
\mathbf{N}'_B\left(x, l_{eB}(t)\right) &= \left[\ N'_{B,1}\ N'_{B,2}\ N'_{B,3}\ N'_{B,4}\ \right] \otimes \mathbf{I}_4 \\
\mathbf{N}''_B\left(x, l_{eB}(t)\right) &= \left[\ N''_{B,1}\ N''_{B,2}\ N''_{B,3}\ N''_{B,4}\ \right] \otimes \mathbf{I}_4
\end{aligned}
\tag{32}
$$

where

$$
\begin{aligned}
N'_{B,1}(\xi_B) &= 6\left(-\xi_B + \xi_B^2\right)/l_{eB}, \\
N'_{B,2}(\xi_B) &= \left(1 - 4\xi_B + 3\xi_B^2\right), \\
N'_{B,3}(\xi_B) &= 6\left(\xi_B - \xi_B^2\right)/l_{eB}, \\
N'_{B,4}(\xi_B) &= \left(3\xi_B^2 - 2\xi_B\right)
\end{aligned}
$$

$$
\begin{aligned}
N''_{B,1}(\xi_B) &= -6\left(1 - 2\xi_B\right)/l_{eB}^2, \\
N''_{B,2}(\xi_B) &= \left(-4 + 6\xi_B\right)/l_{eB}, \\
N''_{B,3}(\xi_B) &= 6\left(1 - 2\xi_B\right)/l_{eB}^2, \\
N''_{B,4}(\xi_B) &= \left(6\xi_B - 2\right)/l_{eB}
\end{aligned}
$$

$\mathbf{M}_{vL}$ and $\mathbf{M}_{vR}$ are total mass matrices of left and right hoisting ropes:

$$
\begin{aligned}
\mathbf{M}_{vL} &= \sum_{k=1}^{n_{vL}} \left(\mathbf{B}^H\right)^T \mathbf{M}_{evL} \mathbf{B}^H, \\
\mathbf{M}_{vR} &= \sum_{k=1}^{n_{vR}} \left(\mathbf{B}^H\right)^T \mathbf{M}_{evR} \mathbf{B}^H \\
\mathbf{M}_{evL} &= \rho_2 l_{evL} \int_0^1 \left(\mathbf{N}_{vL}\right)^T \mathbf{N}_{vL}\, d\xi_{vL}, \\
\mathbf{M}_{evR} &= \rho_3 l_{evR} \int_0^1 \left(\mathbf{N}_{vR}\right)^T \mathbf{N}_{vR}\, d\xi_{vR}
\end{aligned}
$$

$\mathbf{C}_{vL}$ and $\mathbf{C}_{vR}$ are total damping matrices of left and right hoisting ropes:

$$\mathbf{C}_{vL} = \sum_{k=1}^{n_{vL}} \left(\mathbf{B}^H\right)^T \mathbf{C}_{evL} \mathbf{B}^H,$$

$$\mathbf{C}_{vR} = \sum_{k=1}^{n_{vR}} \left(\mathbf{B}^H\right)^T \mathbf{C}_{evR} \mathbf{B}^H$$

$$\mathbf{C}_{evL} = l_{evL} \sum_{i=1}^{N_{vL}} \int_0^1 (\rho_2(2\mathbf{N}_{vL}^T\dot{\mathbf{N}}_{vL} + v_{vL}\mathbf{N}_{vL}^T\mathbf{N}'_{vL}$$
$$-v_{vL}\mathbf{N}'^T_{vL}\mathbf{N}_{vL}) + \zeta_v Q_{a2}\mathbf{N}_{vL}^T\mathbf{N}'_{vL})\mathrm{d}\xi_{vL}$$

$$\mathbf{C}_{evR} = l_{evR} \sum_{i=1}^{N_{vR}} \int_0^1 (\rho_3(2\mathbf{N}_{vR}^T\dot{\mathbf{N}}_{vR} + v_{vR}\mathbf{N}_{vR}^T\mathbf{N}'_{vR}$$
$$-v_{vR}\mathbf{N}'^T_{vR}\mathbf{N}_{vR}) + \zeta_v Q_{a3}\mathbf{N}_{vR}^T\mathbf{N}'_{vR})\mathrm{d}\xi_{vR}$$

$\mathbf{K}_{vL}$ and $\mathbf{K}_{vR}$ are total stiffness matrices of left and right hoisting ropes:

$$\mathbf{K}_{vL} = \sum_{k=1}^{n_{vL}} \left(\mathbf{B}^H\right)^T \mathbf{K}_{evL} \mathbf{B}^H,$$

$$\mathbf{K}_{vR} = \sum_{k=1}^{n_{vR}} \left(\mathbf{B}^H\right)^T \mathbf{K}_{evR} \mathbf{B}^H$$

$$\mathbf{K}_{evL} = l_{evL} \sum_{i=1}^{N_{vL}} \int_0^1 (\rho_2 v_{vL}(\mathbf{N}_{vL}^T\dot{\mathbf{N}}'_{vL} + \dot{\mathbf{N}}_{vL}^T\mathbf{N}'_{vL}$$
$$- 2\mathbf{N}'^T_{vL}\dot{\mathbf{N}}_{vL} - v_{vL}\mathbf{N}'^T_{vL}\mathbf{N}'_{vL})$$
$$+ \rho_2(\mathbf{N}_{vL}^T\ddot{\mathbf{N}}_{vL} + a_{vL}\mathbf{N}_{vL}^T\mathbf{N}'_{vL}) + Q_{a2}\mathbf{N}'^T_{vL}\mathbf{N}'_{vL})\mathrm{d}\xi_{vL}$$

$$\mathbf{K}_{evR} = l_{evR} \sum_{i=1}^{N_{vR}} \int_0^1 (\rho_3 v_{vR}(\mathbf{N}_{vR}^T\dot{\mathbf{N}}'_{vR} + \dot{\mathbf{N}}_{vR}^T\mathbf{N}'_{vR}$$
$$- 2\mathbf{N}'^T_{vR}\dot{\mathbf{N}}_{vR} - v_{vR}\mathbf{N}'^T_{vR}\mathbf{N}'_{vR})$$
$$+ \rho_3(\mathbf{N}_{vR}^T\ddot{\mathbf{N}}_{vR} + a_{vR}\mathbf{N}_{vR}^T\mathbf{N}'_{vR}) + Q_{a3}\mathbf{N}'^T_{vR}\mathbf{N}'_{vR})\mathrm{d}\xi_{vR}$$

Data availability The data are available from the corresponding author on reasonable request.

Declarations

Conflicts of Interest The authors declare that there are no conflicts of interest regarding the publication of this paper.

References

1. Chen X, Zhu Z, Ma T, Shen G (2022) Model-based sensor fault detection, isolation and tolerant control for a mine hoist. Measurement and Control 55(5–6):274–287. https://doi.org/10.1177/00202940221090549
2. Wang J, Pi Y, Hu Y, Gong X (2017) Modeling and dynamic behavior analysis of a coupled multi-cable double drum winding hoister with flexible guides. Mech Mach Theory 108:191–208. https://doi.org/10.1016/j.mechmachtheory.2016.10.021
3. Wang Y, Zhu W, Kou Z (2022) Dynamic simulation of a dual-cable parallel winding hoisting system with flexible guides. Int J Struct Stab Dynam. https://doi.org/10.1142/S0219455422500183
4. Stefan K, Ostachowicz W (2003) Transient vibration phenomena in deep mine hoisting cables. Part 1: Mathematical model. J Sound Vib 262:219–244. https://doi.org/10.1016/S0022-460X(02)01137-9
5. Wang L, Cao G, Wang N, Yan L (2019) Modeling and dynamic behavior analysis of rope-guided traction system with terminal tension acting on compensating rope. Shock Vib. 2019, doi: https://doi.org/10.1155/2019/6362198
6. Wang N, Cao G, Yan L, Wang L (2019) Modelling and passive control of flexible guiding hoisting system with time-varying length. Math Comput Model Dyn Syst 26:1–24. https://doi.org/10.1080/13873954.2019.1699121
7. Yan L, Cao G, Wang N, Peng W (2020) Schematic diagrams design of displacement suppression mechanism with one degree-of-freedom in a rope-guided hoisting system. Symmetry 12:474. https://doi.org/10.3390/sym12030474
8. Zhou P, Zhou G, Zhu Z, Tang C, He Z, Li W, Jiang F (2018) Health monitoring for balancing tail ropes of a hoisting system using a convolutional neural network. Appl Sci 8:1346. https://doi.org/10.3390/app8081346
9. Zhu W, Ren H, Xiao C (2010) A nonlinear model of a slack cable with bending stiffness and moving ends with application to elevator traveling and compensation cables. Dynam Syst Control 8:1137–1163. https://doi.org/10.1115/IMECE2010-39219
10. Feyrer K (2007) Wire ropes: tension, endurance, reliability. Springer, Berlin. https://doi.org/10.1007/978-3-540-33831-4
11. Song Z, Wang X, Li Y, Guo Y, Hao H, Huang J (2022) Co-simulation model coupling of flexible rope hoisting system and hydraulic braking system for a mine hoist. Proc Inst Mech Eng 236(3):881–893. https://doi.org/10.1177/09544089211053521
12. Cao G, Wang J, Zhu Z, Wang Y, Peng W (2015) Lateral response and energetics of cable-guided hoisting system with time-varying length. Journal of Vibroengineering 17:4575–4588
13. Wang Y, Cao G, van Horssen WT (2018) Dynamic simulation of a multi-cable driven parallel suspension platform with slack cables. Mech Mach Theory 126:329–343. https://doi.org/10.1016/j.mechmachtheory.2018.04.014
14. Cao G, Cai X, Wang N, Peng W, Li J (2017) Dynamic response of parallel hoisting system under drive deviation between ropes with time-varying length. Shock Vib 2017:1–10. https://doi.org/10.1155/2017/6837697
15. Shabana AA, Hussien HA, Escalona JL (1998) Application of the absolute nodal coordinate formulation to large rotation and large deformation problems. J Mech Des 120(2):188–195. https://doi.org/10.1115/1.2826958
16. Shabana A, Yakoub R (2001) Three dimensional absolute nodal coordinate formulation forbeam elements: Theory. J Mech Design 123:606–613. https://doi.org/10.1115/1.1410100
17. Wang Z, Xiang C, Liu H, Liu M (2022) Accuracy and efficiency analysis of the beam elements for nonlinear large deformation. J Vib Eng Technol, doi: https://doi.org/10.1007/s42417-022-00581-1
18. Zhang Y, Guo J, Liu Y, Wei C (2021) Absolute nodal coordinate formulation based decoupled-stranded model for flexible cables with large deformation. J Comput Nonlinear Dynam. https://doi.org/10.1115/1.4049563

19. Zhang N, Cao G, Yang F (2021) Dynamic analysis of balance rope under multiple constraints with friction. Proc Inst Mech Eng C J Mech Eng Sci 235(24):7412–7429. https://doi.org/10.1177/0954406220986599

20. Fan W, Zhu WD, Ren H (2016) A new singularity-free formulation of a three dimensional euler-bernoulli beam using euler parameters. J Comput Nonlinear Dynam. https://doi.org/10.1115/1.4031769

21. Fan W, Zhu W (2017) Dynamic analysis of an elevator traveling cable using a singularity-free beam formulation,doi: https://doi.org/10.1115/DETC2017-68299

22. Xia J, Cao G, Wang Y, Peng W (2014) Study on multicharacteristic of antirotation wire rope based on linear stiffness coefficient. Adv Mech Eng 2014:1–10. https://doi.org/10.1155/2014/512627

23. Dombrowski S (2002) Analysis of large flexible body deformation in multibody systems using absolute coordinates. Multibody SysDyn 8:409–432. https://doi.org/10.1023/A:1021158911536

24. Yang S, Hu H, Mo G, Zhang X, Qin J, Yin S, Zhang J (2021) Dynamic modeling and analysis of an axially moving and spinning rayleigh beam based on a time-varying element. Appl Math Model 95:409–434. https://doi.org/10.1016/j.apm.2021.01.049

25. Wang J, Cao G, Zhu Z, Wang Y, Peng W (2015) Lateral response of cable-guided hoisting system with time-varying length: Theoretical model and dynamics simulation verification. Proc Inst Mech Eng C J Mech Eng Sci 229:2908–2920. https://doi.org/10.1177/0954406214566032

26. Costello GA (1992) Theory of wire rope. Mech Eng doi: https://doi.org/10.1007/978-1-4684-0350-3

27. Zemljaric B, Azbe V (2019) Analytically derived matrix end-form elastic-forces equations for a low-order cable element using the absolute nodal coordinate formulation. J Sound Vib 446:263–272. https://doi.org/10.1016/j.jsv.2019.01.039

28. Ebrahimi M, Butscher A, Cheong H (2021) A low order, torsion deformable spatial beam element based on the absolute nodal coordinate formulation and bishop frame. Multibody SysDyn 51:1–32. https://doi.org/10.1007/s11044-020-09765-7

29. Shabana AA (2017) Computational continuum mechanics Third Edition, pp. 1–368, doi: https://doi.org/10.1002/9781119293248

30. Zhang R, Yu Y, Wang Q, Wang Q (2020) An improved implicit method for mechanical systems with set-valued friction. Multibody SysDyn 48:1–28. https://doi.org/10.1007/s11044-019-09713-0

31. Bulín R, Hajžman M, Polach P (2017) Nonlinear dynamics of a cable-pulley system using the absolute nodal coordinate formulation. Mech Res Commun 82:21–28. https://doi.org/10.1016/j.mechrescom.2017.01.001

32. Kadapa C, Dettmer W, Perić D (2017) On the advantages of using the first-order generalised-alpha scheme for structural dynamic problems. Comput Struct 193:226–238. https://doi.org/10.1016/j.compstruc.2017.08.013

33. Zhang, N., Cao, G., Wang, K.: Research on the time-varying elements of balance rope in friction hoisting system for vertical shaft. (2021). https://doi.org/10.26914/c.cnkihy.2021.016483. 8th International Conference on Vibration Engineering, Shanghai, China, 144–149 July 2021